# The Journal of Chemical Physics

## Enhanced Li-ion diffusion and electrochemical performance in strained-manganese-iron oxide core-shell nanoparticles

Cite as: J. Chem. Phys. 155, 144702 (2021); https://doi.org/10.1063/5.0065506 Submitted: 02 August 2021 • Accepted: 21 September 2021 • Published Online: 13 October 2021









View Online





### Enhanced Li-ion diffusion and electrochemical performance in strained-manganese-iron oxide core-shell nanoparticles

Cite as: J. Chem. Phys. 155, 144702 (2021); doi: 10.1063/5.0065506 Submitted: 2 August 2021 • Accepted: 21 September 2021 • Published Online: 13 October 2021







Anuj Bhargava,<sup>1</sup> D Yuval Elbaz,<sup>2</sup> Quynh Sam,<sup>1</sup> D Michelle A. Smeaton,<sup>1</sup> Lena F. Kourkoutis,<sup>3,4</sup> D

Maytal Caspary Toroker, 2.5 and Richard D. Robinson 1.8 b

### **AFFILIATIONS**

- Department of Materials Science and Engineering, Cornell University, Ithaca, New York 14853, USA
- <sup>2</sup>Department of Materials Science and Engineering, Technion–Israel Institute of Technology, Haifa 3200003, Israel
- <sup>3</sup>School of Applied and Engineering Physics, Cornell University, Ithaca, New York 14853, USA
- <sup>4</sup>Kavli Institute for Nanoscale Science, Cornell University, Ithaca, New York 14853, USA
- <sup>5</sup>The Nancy and Stephen Grand Technion Energy Program, Technion—Israel Institute of Technology, Haifa 3200003, Israel

Note: This paper is part of the JCP Special Topic on Transport of Charge and Energy in Low-Dimensional Materials.

a) Author to whom correspondence should be addressed: rdr82@cornell.edu

### **ABSTRACT**

Efforts to improve energy storage depend greatly on the development of efficient electrode materials. Recently, strain has been employed as an alternate approach to improve ion mobility. While lattice strain has been well-researched in catalytic applications, its effects on electrochemical energy storage are largely limited to computational studies due to complexities associated with strain control in nanomaterials as well as loss of strain due to the phase change of the active material during charging–discharging. In this work, we overcome these challenges and investigate the effects of strain on supercapacitor performance in Li-ion-based energy devices. We synthesize epitaxial  $Fe_3O_4@MnFe_2O_4$  (core@shell) nanoparticles with varying shell thickness to control the lattice strain. A narrow voltage window for electrochemical testing is used to limit the storage mechanism to lithiation–delithiation, preventing a phase change and maintaining structural strain. Cyclic voltammetry reveals a pseudocapacitive behavior and similar levels of surface charge storage in both *strained*- and *unstrained*-MnFe $_2O_4$  samples; however, diffusive charge storage in the strained sample is twice as high as the unstrained sample. The *strained*-MnFe $_2O_4$  electrode exceeds the performance of the *unstrained*-MnFe $_2O_4$  electrode in energy density by  $\sim 33\%$ , power density by  $\sim 28\%$ , and specific capacitance by  $\sim 48\%$ . Density functional theory shows lower formation energies for Li-intercalation and lower activation barrier for Li-diffusion in *strained*-MnFe $_2O_4$ , corresponding to a threefold increase in the diffusion coefficient. The enhanced Li-ion diffusion rate in the strained-electrodes is further confirmed using the galvanostatic intermittent titration technique. This work provides a starting point to using strain engineering as a novel approach for designing high performance energy storage devices.

Published under an exclusive license by AIP Publishing. https://doi.org/10.1063/5.0065506

### INTRODUCTION

Nanostructured materials have played a crucial role in the development of next-generation electrochemical energy storage devices. Unique properties emerge in nanoscale materials, and often, those properties can be tuned to optimize electrochemical performance. Among the most important tunable parameters are the surface-to-volume ratio and short diffusion path lengths, which lead to improvements in energy density, charge/discharge rates, and

cycling stability in electrode materials.<sup>1</sup> In recent years, nanomaterials engineering has expanded to include strain engineering.<sup>2,3</sup> The presence of lattice strain has been shown to alter the surface interatomic distance, thereby improving ion mobility and diffusion.<sup>4,5</sup> Theoretical calculations find that the diffusion coefficient for Li-ions in LiCoO<sub>2</sub> increases with increasing interfacial strain,<sup>6</sup> and atomistic simulations conducted reveal that tensile strain reduces the migration barrier for both Li<sup>+</sup> and Na<sup>+</sup> ions in olivine type phosphate.<sup>7</sup>

The number of studies investigating the influence of lattice strain on electrochemical energy conversion and storage has greatly increased in recent years; however, much of the literature is limited to computational methods<sup>4</sup> due to various experimental challenges.8 Previously, a report by Muralidharan et al. demonstrated that increasing mechanical strain in V<sub>2</sub>O<sub>5</sub> films grown on NiTi alloy substrates via atomic layer deposition (ALD) improved lithium diffusion but lacked key electrochemical parameters such as energy and power density and specific capacitance.8 More comprehensive studies have been performed on multiple 2D layered materials. In Ti<sub>3</sub>C<sub>2</sub>T<sub>x</sub> MXenes, mechanochemically induced strain resulted in higher discharge capacity and improved rate capability. The strain induced by the interlayer lattice mismatch has been reported to enhance Li-ion intercalation and electrochemical performance in carbon-MoS<sub>2</sub> nanosheets and VOPO<sub>4</sub>-graphene heterostructures. 10,11 Strain engineering has also been successfully carried out using core-shell particles in several studies; however, the impact on performance has been explored primarily in catalytic applications.<sup>12</sup> The relationship between the strain and the electrochemical performance of Li-ion storage devices is not often directly investigated due to (1) the onset of conversion reactions during charge-discharge, which leads to phase changes in the active material and (2) the complexity of controlling lattice strain in nanomaterials.<sup>13</sup> Phase changes, often associated with slow charge transfer kinetics, alter the atomic structure and eliminate any induced strain. In this work, we overcome the aforementioned challenges to demonstrate an increase in the supercapacitor performance for a quantifiable amount of strain. Strain control is achieved using core@shell heterostructures, where the epitaxial interface can be leveraged for this purpose. 13,14 The tuning of these parameters to create strain engineered core@shell materials greatly expands the options for improving energy storage and conversion.

A large number of Li-ion-based energy storage devices are comprised of spinel-based components, such as electrodes and electrolytes. <sup>15</sup> Spinels are a widely studied and versatile class of materials that allow for lattice matching to reduce interfacial resistance. <sup>16</sup> For these reasons, spinels are an ideal system to use for investigating the relationship between the lattice strain and the electrochemical performance. In this study, we devise a synthesis method to grow epitaxially *strained*-Fe<sub>3</sub>O<sub>4</sub>@MnFe<sub>2</sub>O<sub>4</sub> (core@shell) nanoparticles (NPs) and *unstrained*-MnFe<sub>2</sub>O<sub>4</sub> as a control to investigate the effects of strain on Li-ion transport and electrochemical

performance. The MnFe<sub>2</sub>O<sub>4</sub> ternary spinel system is chosen for this study because among the ferrite ternary spinel systems, MnFe<sub>2</sub>O<sub>4</sub> has been shown to have highest specific capacitance, 17 making it a potential active material for energy storage applications. Fe<sub>3</sub>O<sub>4</sub> is used as the core material for two reasons. First, Fe<sub>3</sub>O<sub>4</sub> has the highest electronic conductivity among the ferrite spinels (10<sup>3</sup> S/cm).<sup>18</sup> Second, the lattice parameter of Fe<sub>3</sub>O<sub>4</sub> (8.397 Å) is similar to the MnFe<sub>2</sub>O<sub>4</sub> lattice parameter (8.515 Å), which facilitates synthesis of epitaxially strained core@shell structures. In addition, epitaxial growth prevents grain boundary formation at the interface of the core and the shell, reducing the barrier for electronic charge transport. 19 By designing a hybrid core@shell structure, we aim to leverage mixed electronic and electrochemical properties such that more charge can be stored in the electrode to improve the energy density of the active material while simultaneously improving the power density as the charges can be extracted at a faster rate following the redox activity in the active material. Following the synthesis of the NPs, additive-free electrodes are fabricated via electrophoretic deposition (EPD) (Fig. 1). EPD is used because this technique has been shown to produce electrodes with superior gravimetric capacity and electrochemical performance compared to the conventional methods.<sup>20–22</sup> The absence of additives in EPD leads to electrodes with higher density of active material.<sup>20</sup> In addition, NP coatings applied via EPD are mechanically robust with smooth and largely defect-free surfaces that can better facilitate charge transfer kinetics. 20,22 The electrodes are annealed for ligand removal and then assembled into coin cells, and the electrochemical testing voltage window is determined using cyclic voltammograms such that the phase and the strain in the active material are preserved. Subsequently, the supercapacitor performance of the material is evaluated, and a correlation is observed between the strain and the electrochemical performance. The galvanostatic intermittent titration technique (GITT) is used to calculate the Li-ion diffusion rates in the strained and unstrained electrodes. Finally, using density functional theory with the Hubbard correction term (DFT + U), we calculate the activation barriers for Li diffusion and the formation energies for Li-intercalated MnFe<sub>2</sub>O<sub>4</sub>. From our results, we find that the superior supercapacitor performance of strained-MnFe<sub>2</sub>O<sub>4</sub> compared to unstrained-MnFe<sub>2</sub>O<sub>4</sub> can be directly attributed to the accelerated Li-ion diffusion rate in the strained structure. With this work, we provide a novel approach to enhance Li-ion transport and hence design improved, high-performance energy storage devices.

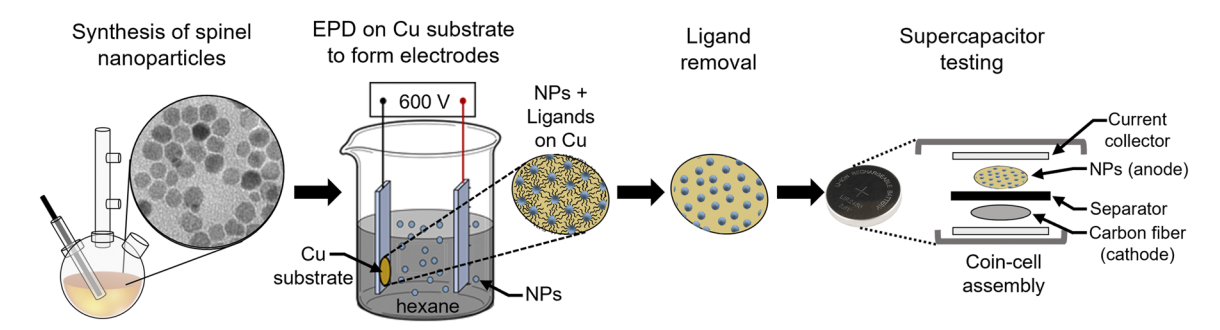


FIG. 1. Experimental approach. Schematic showing the synthesis of spinel nanoparticles (NPs), preparation of additive-free electrodes using electrophoretic deposition (EPD), ligand removal, and supercapacitor performance evaluation.

### **RESULTS AND DISCUSSION**

Thermal decomposition of metallorganic precursors in an organic solvent was employed for NP synthesis.<sup>23</sup> The assynthesized Fe<sub>3</sub>O<sub>4</sub> and MnFe<sub>2</sub>O<sub>4</sub> NPs have a spherical morphology with diameters of 5.9 nm ( $\pm 10\%$ ) and 5.6 nm ( $\pm 16\%$ ), respectively [Fig. 2(a)]. To grow the epitaxial core@shell NPs, MnFe<sub>2</sub>O<sub>4</sub> is grown as a shell material on solid Fe<sub>3</sub>O<sub>4</sub> cores with varying shell thickness {i.e., no shell, 1.35 nm shells, and 2.70 nm shells [Fig. 2(b)]} (see experimental section in the supplementary material for details). Higher levels of strain were not studied because further increasing the shell thickness leads to MnFe<sub>2</sub>O<sub>4</sub> nucleating separately instead of depositing as a shell during the synthesis. High-angle annular dark-field scanning transmission electron microscopy (HAADF-STEM) images of Fe<sub>3</sub>O<sub>4</sub>@ 2.70 nm-MnFe<sub>2</sub>O<sub>4</sub> NPs show an epitaxial shell growth with no discernible defects [Fig. 2(c)]. A clear distinction can be made between the core and the shell using elemental mapping with electron energy loss spectroscopy (EELS), which is consistent with an Fe-rich core and the distribution of both Mn and Fe cations in the shell [Fig. 2(c)]. Elemental intensity line profiles taken across the NP exhibit the expected distribution of Mn and Fe cations [white dashed box in Fig. 2(d) and corresponding plot in Fig. 2(e)]. Projection of the electron probe through the NP leads to a flat Mn profile across the core of the NP (produced by interaction with the shell on the top and bottom surfaces) with a relative increase at either edge, where the projected thickness of the shell increases [Fig. 2(e)]. The estimated Mn to Fe ratio

across the nanoparticle is found to be consistent with the Mn to Fe ratio calculated using EELS (Fig. S1 and calculation), indicating the core stoichiometry as Fe<sub>3</sub>O<sub>4</sub> and the shell stoichiometry as MnFe<sub>2</sub>O<sub>4</sub>. The stoichiometry of the shell is quantified using inductively coupled plasma mass spectrometry (ICP-MS) analysis (Table S1, see the supplementary material for details) as Mn<sub>1.06</sub>Fe<sub>1.94</sub>O<sub>4</sub> and Mn<sub>1.31</sub>Fe<sub>1.69</sub>O<sub>4</sub> for the thin- and thickshelled core@shell samples, respectively (assuming no interdiffusion of Mn into the core). Since the two shell stoichiometries  $x \sim 1$  and  $x \sim 1.3$  ("x" in Mn<sub>x</sub>Fe<sub>3-x</sub>O<sub>4</sub>) have similar cation site occupation, electronic conductivity, 18 and concentration of Mn and Fe species [confirmed using x-ray photoemission spectroscopy (XPS) analysis on the core@shell NPs used in this study, Fig. S3 and Table S4], we disregard the role of slight deviation in shell stoichiometries on the electrochemical performance. For further reference, both the shell stoichiometries are assumed to be as MnFe<sub>2</sub>O<sub>4</sub>.

X-ray diffraction (XRD) measurements confirm the phase of the annealed NPs (solid cores and the core@shell NPs) as spinel and further show an evolution of the strain in the NPs with an increasing shell thickness. The XRD characterization and the subsequent strain measurements are carried out on the annealed (ligand-removed) nanoparticles so that the processing conditions of the nanoparticles are consistent between the structural and electrochemical characterizations. The XRD peak intensity and positions of the annealed solid NPs [Fig. 3(a), black and green] match the bulk standards for MnFe<sub>2</sub>O<sub>4</sub> (JCPDS: 01-073-1964) and Fe<sub>3</sub>O<sub>4</sub>

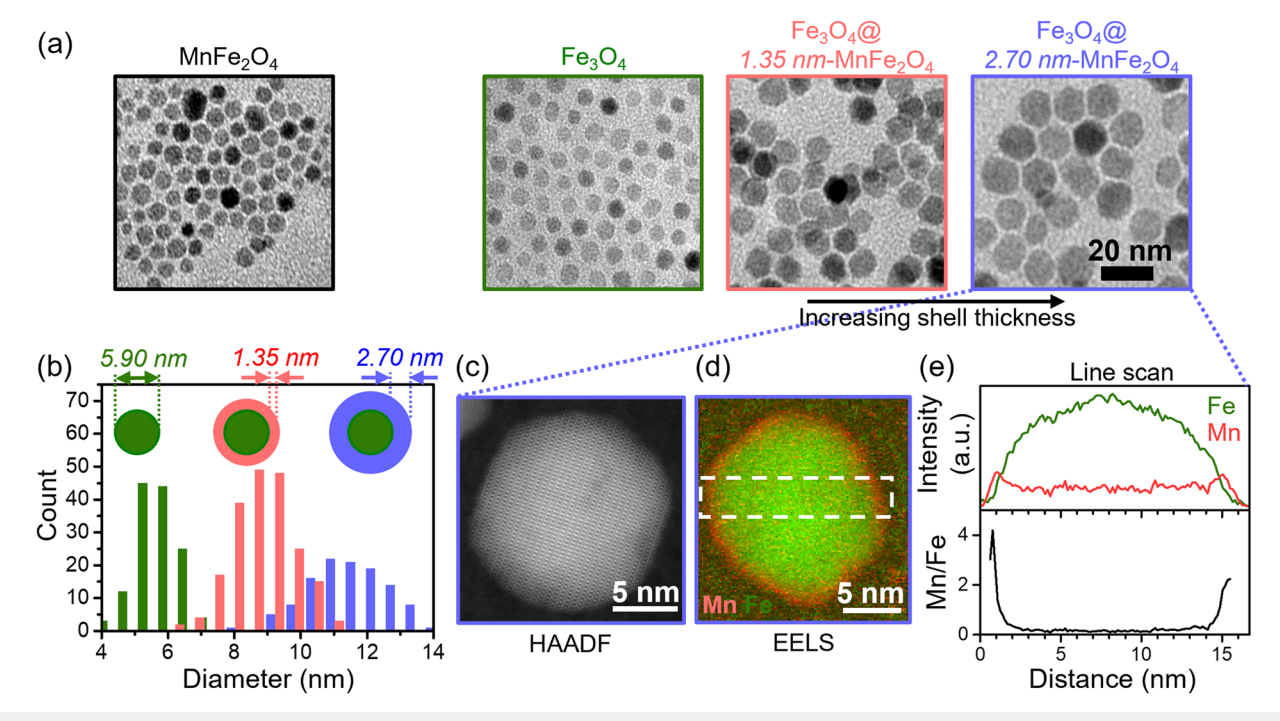


FIG. 2. (a) Transmission electron microscopy for the characterization of nanoparticles (NPs)—MnFe $_2$ O $_4$ , Re $_3$ O $_4$ , and core@shell Fe $_3$ O $_4$ @MnFe $_2$ O $_4$  with a shell thickness of 1.35 and 2.70 nm. (b) Histogram showing the size of the core (green) and the NP after the shell growth. (c) High-angle annular dark-field scanning transmission electron microscopy (HAADF-STEM) image of an Fe $_3$ O $_4$ @ 2.70 nm-MnFe $_2$ O $_4$  NP. Crystalline ordering extends fully to the edges of the NP and no delineation between the core and the shell is visible, indicating epitaxial growth. (d) EELS elemental map of another Fe $_3$ O $_4$ @ 2.70 nm-MnFe $_2$ O $_4$  NP showing the distribution of Mn (red) and Fe (green) within the NP. The core is Fe-rich, whereas the shell is found to be a mix of Mn and Fe. (e) Mn and Fe line profiles (top) and the ratio of Mn and Fe (bottom) across the NP, as indicated by the white dashed box on the elemental map.

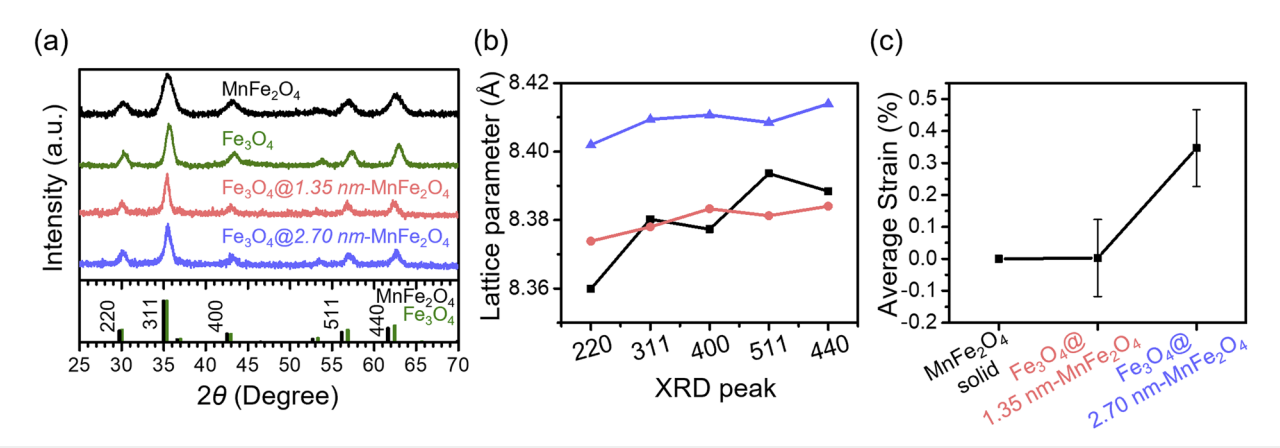


FIG. 3. (a) X-ray diffraction (XRD) to confirm the phase of annealed nanoparticles. The bar patterns show the reference XRD patterns for MnFe<sub>2</sub>O<sub>4</sub> (JCPDS: 01-073-1964) and Fe<sub>3</sub>O<sub>4</sub> (JCPDS: 00-019-0629). All XRD patterns align well with the reference patterns, indicating that the nanoparticles are in the spinel phase with no impurities. (b) Lattice parameter extracted via Lorentz profile fitting of the XRD peaks assuming a cubic unit cell. (c) Strain in the nanoparticles calculated with respect to the solid MnFe<sub>2</sub>O<sub>4</sub> nanoparticles. The strain and error bars correspond to the average strain along different planes and the standard deviation, respectively.

(JCPDS: 00-019-0629), confirming that the NPs are in the spinel phase with no impurities. Following MnFe<sub>2</sub>O<sub>4</sub> shell growth on top of the Fe<sub>3</sub>O<sub>4</sub> cores [Fig. 3(a), red and blue], the phase of the NPs remains as spinel. However, the peaks become narrower (Table S1), indicating an increase in the crystal size of the NPs, which matches the observations from TEM [Fig. 2(a)]. Interestingly, the hybrid Fe<sub>3</sub>O<sub>4</sub>@MnFe<sub>2</sub>O<sub>4</sub> nanoparticle XRD peak positions match with MnFe<sub>2</sub>O<sub>4</sub> rather than Fe<sub>3</sub>O<sub>4</sub>. The shell material occupies 77% and 86% of the total volume within each nanoparticle for the thin-shelled Fe<sub>3</sub>O<sub>4</sub>@ 1.35 nm-MnFe<sub>2</sub>O<sub>4</sub> and the thickshelled Fe<sub>3</sub>O<sub>4</sub>@ 2.70 nm-MnFe<sub>2</sub>O<sub>4</sub> nanoparticles, respectively (see Table S1). Because of the dominance of the MnFe<sub>2</sub>O<sub>4</sub> material over the Fe<sub>3</sub>O<sub>4</sub> and since the core and the shell have an epitaxial interface, it is likely that the Fe<sub>3</sub>O<sub>4</sub> core is also being strained by the MnFe<sub>2</sub>O<sub>4</sub> shell material. The shell material straining the core material is counterintuitive because generally in lattice strain studies, the "core" is a substrate upon which a thin film is grown (i.e., the shell), and in this instance, the substrate is substantive enough to control the lattice parameter of the whole thin film. In our case, however, a much thicker MnFe<sub>2</sub>O<sub>4</sub> shell is grown on top of a very thin Fe<sub>3</sub>O<sub>4</sub> substrate. This volume dominance of the thick shell results in the XRD peaks for the Fe<sub>3</sub>O<sub>4</sub>@MnFe<sub>2</sub>O<sub>4</sub> hybrid shifting to spacings that are closer to the MnFe<sub>2</sub>O<sub>4</sub> pure particles.

Lorentz profile fitting of the XRD peaks [Fig. S2(b)] is used to determine the peak position (Table S2), and subsequently, the lattice parameters are calculated [Fig. 3(b); see the supplementary material for calculation details]. The lattice parameter of the thin-shelled Fe<sub>3</sub>O<sub>4</sub>@ 1.35 nm-MnFe<sub>2</sub>O<sub>4</sub> is nearly identical to the solid MnFe<sub>2</sub>O<sub>4</sub> NPs, whereas the lattice parameter of thick-shelled Fe<sub>3</sub>O<sub>4</sub>@ 2.70 nm-MnFe<sub>2</sub>O<sub>4</sub> [Fig. 3(b)] increases by ~0.03 Å along all crystallographic planes, indicating that the thick-shelled NPs are epitaxially strained. The solid MnFe<sub>2</sub>O<sub>4</sub> 5.6 nm nanoparticle has a lattice parameter of 8.38 Å (Table S3), which is much smaller than the 8.515 Å lattice parameter for bulk-MnFe<sub>2</sub>O<sub>4</sub> (JCPDS: 01-073-1964). However, as the diameter of the nanoparticles increases from 5.60 to 8.30 nm for the hybrid with a shell thickness of 2.7 nm, the d-spacing increases to 8.41 Å, indicating that the MnFe<sub>2</sub>O<sub>4</sub> is

transitioning from a more nanoparticle-like MnFe<sub>2</sub>O<sub>4</sub> lattice to a more bulk-like MnFe<sub>2</sub>O<sub>4</sub> lattice. Similar trends of a decreasing lattice parameter for a decreasing nanoparticle diameter have been reported previously for MnFe<sub>2</sub>O<sub>4</sub>, <sup>24,25</sup> but the lattice parameter value is not intrinsically linked to a specific size, with several groups reporting different lattice constants for the same size of nanoparticles.<sup>24–27</sup> For example, nanoparticles of 5 and 6 nm synthesized using a coprecipitation method<sup>24</sup> have the lattice parameter of 8.43 and 8.48 Å, whereas our 5.6 nm solid MnFe<sub>2</sub>O<sub>4</sub> nanoparticle has a lattice parameter of 8.38 Å. This inconsistency indicates that the size of the nanoparticle is not the sole factor controlling the lattice constant and other influences are at play, such as the synthesis conditions, which include the type of terminating ligand groups and the extent or absence of oxygen vacancies.<sup>28</sup> For more quantitative analysis, the strain in the core@shell NPs is calculated with respect to the solid MnFe<sub>2</sub>O<sub>4</sub> NPs lattice parameter values, i.e., assuming that the solid MnFe<sub>2</sub>O<sub>4</sub> NPs are unstrained (see the supplementary material for calculation details). Since the inherent nanoscale lattice parameter is dependent on the synthesis method, choosing bulk-MnFe<sub>2</sub>O<sub>4</sub> as a reference point to calculate the strain may lead to incorrect assumptions of strain values. For our system, we maintain consistent synthesis conditions between the different samples, grow epitaxial MnFe<sub>2</sub>O<sub>4</sub>-shells onto the cores, and have core@shell NPs that consist of a majority MnFe<sub>2</sub>O<sub>4</sub> by volume and resemble MnFe<sub>2</sub>O<sub>4</sub> NPs with varying size and lattice parameters. For these reasons, we chose the 5.6 nm solid MnFe<sub>2</sub>O<sub>4</sub> NPs to use as the unstrained reference point in our study. The strain for each core@shell sample varies among the different lattice directions. Therefore, for comparison of strain between different samples, the average strain and the corresponding error are calculated by averaging the strain values determined along the five different crystallographic directions [Fig. 3(c) and Table S3]. The thin-shelled Fe<sub>3</sub>O<sub>4</sub>@ 1.35 nm-MnFe<sub>2</sub>O<sub>4</sub> has an average strain of zero, whereas the thick-shelled shows an average tensile strain of 0.35%. For further discussion, the thin-shelled NPs with zero average strain are referred to as "unstrained-shell," whereas the other core@shell NPs are referred to as the "strainedshell" samples. No change in the XRD peak positions and width

is observed before and after the annealing of the NPs [Fig. S2(a)], indicating that there is no strain relaxation following the annealing step. With respect to bulk-MnFe<sub>2</sub>O<sub>4</sub> (JCPDS: 01-073-1964), the nanoparticle samples show a negative strain, and the strain decreases with increasing shell thickness (Fig. S9 and Table S7).

Electrochemical evaluation of the electrodes shows a correlation between the supercapacitor performance and the strain in the MnFe<sub>2</sub>O<sub>4</sub> NPs. To evaluate the effects of strain on the supercapacitor performance, electrodes are fabricated by electrophoretic deposition (EPD) of NPs onto a copper substrate. During EPD, parameters such as the concentration of the colloidal nanoparticle solution, applied voltage, distance between the electrodes, and active mass (mass of the nanoparticles after ligand removal) were kept constant for all samples. Because we keep the deposition parameters constant, we can rule out deposition inconsistencies between the electrodes, such as packing density and film thickness. As a result, the variation in the electrochemical properties between the different strained and unstrained NP electrodes can be correlated directly to the intrinsic properties of the nanoparticles. Following fabrication, the electrodes are thermally annealed<sup>29</sup> in N<sub>2</sub> at 300 °C for 2 h (Fig. S4) and then assembled into a two-electrode coin cell for testing.

Cyclic voltammetry (CV) reveals a pseudocapacitive behavior in both the strained- and unstrained-MnFe2O4 electrodes and improved diffusive charge storage capabilities of the strained sample. The voltage window for all electrochemical testing is determined by measuring the CV curves at various voltage windows (Fig. S5). The largest voltage range, which maintains a quasi-rectangular CV curve, is -0.6 to 0.4 V ( $\Delta$ V = 1 V). Distinct redox peaks begin to form beyond 0.4 V [Fig. S5(a)], indicating the occurrence of irreversible conversion reactions.<sup>30</sup> The lower limit is set at -0.6 V to achieve symmetric output anodic and cathodic current densities. The Coulombic efficiency gradually decreases with increasing potential window [Fig. S5(b)]; however, the maximum possible voltage window of 1 V (i.e., -0.6 to 0.4 V) is used to maximize the energy density while also limiting electron transfer processes to reversible Li intercalation. Within the optimum voltage window, the CV curves are measured at scan rates between 10 and 50 mV/s. The quasirectangular shape of the curves [Fig. 4(a)] indicates the pseudocapacitive behavior in all three materials, where both the electric double layer capacitance and faradaic reactions contribute to charge transfer.<sup>30</sup> The strained-MnFe<sub>2</sub>O<sub>4</sub> sample maintains the pseudocapacitive behavior as the scan rate increases [Fig. 4(b)], indicating a retention of capacitive properties. The overall quasi-rectangular shape remains the same, but the peak current increases linearly with the scan rate [Fig. S6(a)], as is typical in pseudocapacitive

To understand the charge transfer kinetics in the *strained*- and *unstrained*-MnFe<sub>2</sub>O<sub>4</sub> electrodes, the capacitive and diffusive components of the total charge stored in the electrodes are determined from the CV curves using the following equation:  $^{20}$ 

$$Q_t = Q_S + Q_d, (1)$$

where  $Q_S$  is the charge stored on the surface by faradaic charge transfer and the electric double layer capacitance and  $Q_d$  is the diffusive charge stored by faradaic charge transfer within the bulk. Surface charge transfer processes take place instantaneously at the interface of the electrode and electrolyte and are therefore independent of the scan rate. Conversely, higher scan rates provide less time for

ions to diffuse through the bulk electrode material, causing diffusive charge storage to decrease with an increasing scan rate. This diffusive behavior can be modeled based on the semi-infinite linear diffusion model and is given by the following equation:<sup>20</sup>

$$Q_d = k v^{-1/2}. \tag{2}$$

A linear relation between the total charge stored and the inverse of the scan rate [Fig. 4(c)] is observed, demonstrating the pseudocapacitive behavior of the electrodes.<sup>30</sup> These curves are linearly fit to extract the values of Q<sub>S</sub> and Q<sub>d</sub> (from the y-intercept and slope, respectively) and are summarized as bar plots at different scan rates [Fig. 4(d)]. At a given scan rate, the surface charge stored (Q<sub>S</sub>) remains consistent (~23 to 25 C/g) between the three sets of nanoparticle electrodes (unstrained-solid MnFe<sub>2</sub>O<sub>4</sub>, unstrained-Fe<sub>3</sub>O<sub>4</sub>@ 1.35 nm-MnFe<sub>2</sub>O<sub>4</sub>, and strained-Fe<sub>3</sub>O<sub>4</sub>@ 2.70 nm-MnFe<sub>2</sub>O<sub>4</sub>). This consistency in Q<sub>S</sub> is expected since all three samples have the same composition (MnFe<sub>2</sub>O<sub>4</sub>) on the surface. In addition, lack of variation in Q<sub>S</sub> indicates that the strain does not affect the surface properties. Conversely, between the two unstrained electrodes, the diffusive charge stored remains constant (~23 C/g @ 10 mV/s); however, the diffusive charge stored is twice as high (~47 C/g@ 10 mV/s) in the strained-Fe<sub>3</sub>O<sub>4</sub>@ 2.70 nm-MnFe<sub>2</sub>O<sub>4</sub> electrodes, which leads to an overall increase in the total charge stored in this electrode. Our calculations (see the supplementary material) show that under the given scan rates, Li-ions can diffuse to a maximum depth of 0.11 nm in the MnFe<sub>2</sub>O<sub>4</sub> shell material, which is much smaller than the overall shell thickness for the core@shell NPs (1.35 and 2.70 nm). Since the Li-ions cannot reach the  $Fe_3O_4$  core, we disregard the role of the Fe<sub>3</sub>O<sub>4</sub> cores in affecting the Q<sub>d</sub> values for the core@shell electrodes.

To better understand the origin of higher diffusive charge storage in the strained-Fe<sub>3</sub>O<sub>4</sub>@ 2.70 nm-MnFe<sub>2</sub>O<sub>4</sub> electrodes, we first look at the mechanism of the faradic charge transfer in MnFe<sub>2</sub>O<sub>4</sub>. It has been previously observed that in the spinels, up to two Li<sup>+</sup> ions can diffuse without initiating the irreversible conversion reaction.<sup>31</sup> Furthermore, the absence of distinct peaks in the CV curves and the absence of a voltage plateau in the constant current density discharge curves [Fig. S6(b)] of our materials indicate that no irreversible charge transfer processes are occurring.<sup>30</sup> Consequently, we expect that only the following reversible reaction takes place in our material:

$$MnFe_2O_4 + 2Li^+ + 2e^- \rightarrow Li_2MnFe_2O_4.$$
 (3)

From the measured diffusive capacities of the shell samples, we calculate that 0.13 Li $^+$  ions per formula unit intercalate within the strained shell sample, while only 0.08 Li $^+$  ions per formula unit intercalate within the *unstrained*-shell sample (see the supplementary material). The ability of the *strained*-MnFe<sub>2</sub>O<sub>4</sub> sample to accommodate more Li $^+$  ions gives rise to higher diffusive charge storage. To further ensure that there is no contribution from the Fe<sub>3</sub>O<sub>4</sub> core, we use the diffusive capacity to calculate the intercalation depth assuming maximum intercalation of two Li $^+$  ions per formula unit of the spinel (see the supplementary material). The intercalation depth is calculated to be 0.108 nm in *strained*-Fe<sub>3</sub>O<sub>4</sub>@ 2.70 nm-MnFe<sub>2</sub>O<sub>4</sub> NPs and 0.041 nm in the *unstrained*-Fe<sub>3</sub>O<sub>4</sub>@ 1.35 nm-MnFe<sub>2</sub>O<sub>4</sub> NPs. We conclude that the diffusive charge capacity in our materials is attributed entirely to the MnFe<sub>2</sub>O<sub>4</sub> shell and improved by the strain effects.

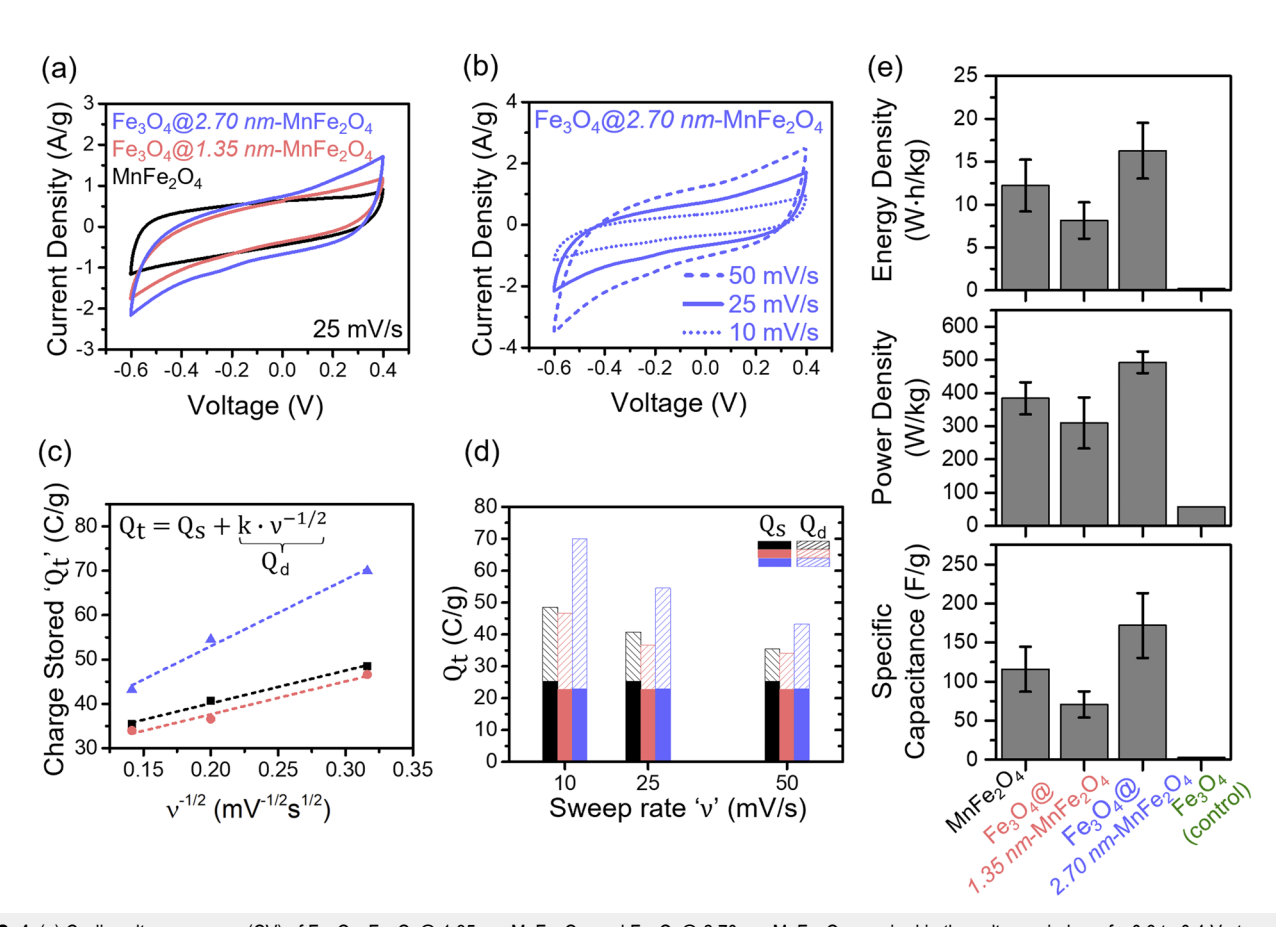


FIG. 4. (a) Cyclic voltammograms (CV) of Fe $_3$ O $_4$ (@ 1.35 nm-MnFe $_2$ O $_4$ , and Fe $_3$ O $_4$ (@ 2.70 nm-MnFe $_2$ O $_4$  acquired in the voltage window of -0.6 to 0.4 V at a scan rate of 25 mV/s. (b) CV of Fe $_3$ O $_4$ (@ 2.70 nm-MnFe $_2$ O $_4$  collected at 50, 25, and 10 mV/s. (c) Total gravimetric charge stored (Q $_t$ ) plotted against the reciprocal of the square root of the potential sweep rate ( $v^{-1/2}$ ) to extract the surface capacitive charge (Q $_s$ ) and diffusive-controlled charge (Q $_t$ ). The inset shows the equation for the relationship between Q $_t$ , Q $_s$ , and Q $_t$ . (d) Illustration of the contribution of Q $_t$ s (solid bars) and Q $_t$ d (striped bars) to the total charge stored at different voltage sweep rates. At a given voltage sweep rate, the three nanoparticle samples have the same amount of surface charge stored (Q $_s$ ), whereas the *strained*-MnFe $_t$ O $_t$ s sample (blue striped bars) is found to have twice the amount of diffusive charge stored as compared to the *unstrained*-MnFe $_t$ O $_t$ s samples (black and red striped bars). (e) Calculated values of energy density, power density, and specific capacitance for the *unstrained*-MnFe $_t$ O $_t$ s and the power density values were obtained by discharging the cells at a fixed current density of 0.1 A/g, and the power density values were obtained by discharging the cells within ~15 s. The *strained*-Fe $_t$ O $_t$ 0 electrodes show an improvement as compared to the *unstrained*-MnFe $_t$ O $_t$ 0 electrodes.

To further compare the electrochemical performance of the strained- and unstrained-samples, constant current density charge-discharge is carried out on the MnFe<sub>2</sub>O<sub>4</sub> samples as well as an Fe<sub>3</sub>O<sub>4</sub> control. The discharge profiles [Fig. S6(b)] show an initial sharp voltage decrease, which corresponds to high resistance to charge transfer as ions have not fully accessed the redox-active material.<sup>20</sup> At lower voltages, the curve becomes more linear, demonstrating that both the double layer capacitance and faradaic charge transfer contribute equally to the discharge process.<sup>20</sup> The absence of plateaus in the curves provides further evidence that only the reversible lithiation reactions are taking place within the set voltage window. 31 The energy density and specific capacitance values are obtained by discharging the cells at a fixed current density of 0.1 A/g, and the power density values are obtained by discharging the cells within ~15 s [Fig. 4(e)]. Across all three performance parameters, the strained-MnFe<sub>2</sub>O<sub>4</sub> sample outperforms the pure MnFe<sub>2</sub>O<sub>4</sub> sample by ~20% and the  $\textit{unstrained}\text{-Fe}_3O_4@1.35~\text{nm-MnFe}_2O_4$  sample

by up to 100%. Measurements of the Fe<sub>3</sub>O<sub>4</sub> control find almost no energy or power density and a very low specific capacitance. Due to the poor performance of the Fe<sub>3</sub>O<sub>4</sub> control and unstrained-MnFe<sub>2</sub>O<sub>4</sub>, the core likely has a negligible contribution to the electrochemical activity of our samples. In order to account for the lack of activity from the Fe<sub>3</sub>O<sub>4</sub> core, we normalize the energy density, power density, and specific capacitance values using the fractional mass of MnFe<sub>2</sub>O<sub>4</sub> in the NP (Fig. S7). The normalized data show similar performance between the pure and unstrained-MnFe<sub>2</sub>O<sub>4</sub> samples, which we believe to be a more accurate representation. The performance of the strained-MnFe<sub>2</sub>O<sub>4</sub> further improves across all three criteria once the core contribution is removed, demonstrating the effect of strain on the electrochemical performance. The improved charge transfer kinetics is further evidenced by the low charge transfer resistance [Fig. S6(c)] in the strained-Fe<sub>3</sub>O<sub>4</sub>@ 2.70 nm-MnFe<sub>2</sub>O<sub>4</sub> (23  $\Omega$ ) as compared to the solid MnFe<sub>2</sub>O<sub>4</sub> electrodes (69  $\Omega$ ); see the supplementary material for details. The cycling performance of

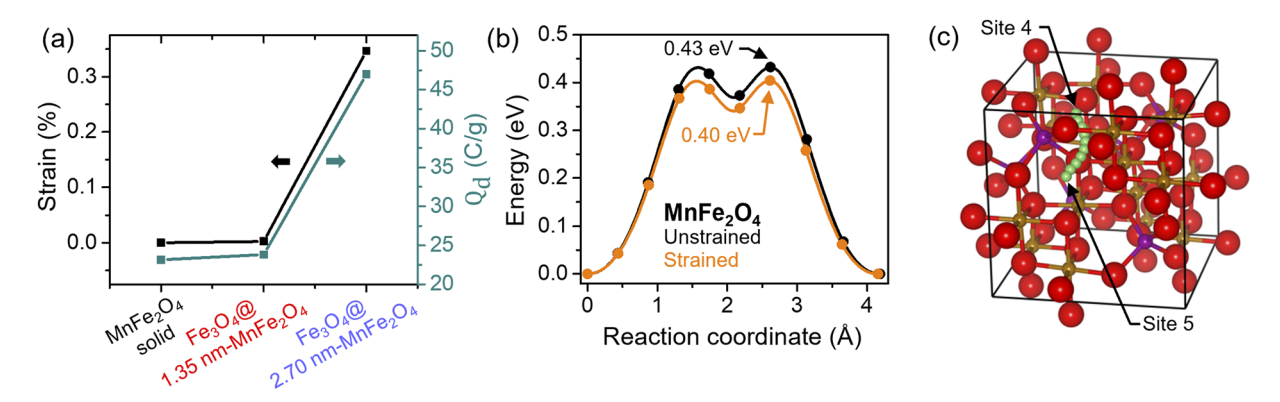


FIG. 5. (a) Correlation between the strain and the diffusive charge stored (calculated at a sweep rate of 10 mV/s) in MnFe<sub>2</sub>O<sub>4</sub>. (b) Activation barriers for Li diffusion in Mn<sub>8</sub>Fe<sub>16</sub>O<sub>32</sub> from a 16c octahedral site to a neighboring 16c site in *unstrained- (black)* and *strained-* (orange) unit cells. The activation energy for Li diffusion is lowered by 0.028 eV in the 0.33% strained cell. (c) Mn<sub>8</sub>Fe<sub>16</sub>O<sub>32</sub> unit cell with the diffusion pathway of the Li-ion. Red—oxygen, gold—iron, magenta—manganese, and green—lithium. Each Li represents the diffusion pathway from the initial to final sites, site 4 to site 5 (Table S6), respectively.

the core@shell electrodes measured at a current density of 0.5 A/g shows a >70% retention in energy density and ~99% Coulombic efficiency after 1000 cycles [Figs. S6(d) and S6(e)], highlighting the cyclic stability and the robustness of the electrodes made via EPD.

A strong correlation is observed between the strain in the MnFe<sub>2</sub>O<sub>4</sub> electrodes [Fig. 5(a), black plot] and the diffusive charge stored [Fig. 5(a), jade plot]. To understand the observed correlation, the formation and activation energies for lithium diffusion are calculated using DFT + U. The modeling is performed using two MnFe<sub>2</sub>O<sub>4</sub> cubic crystal structures with the lattice parameters of 8.38 and 8.41 Å [obtained from XRD results, Fig. 3(b)] to represent the *unstrained*- and *strained*-MnFe<sub>2</sub>O<sub>4</sub>, respectively. The 8.41 Å lattice parameter produces a structure that is strained by 0.33% in all directions relative to the unstrained structure. Formation energies of a single Li intercalation in the supercell are calculated according to the following equation:

$$E_{f} = E_{Li_{0.125}MnFe_{2}O_{4}} - E_{MnFe_{2}O_{4}} - E_{Li},$$
(4)

where  $E_{\text{Li}_{0.125}\text{MnFe}_2\text{O}_4}$  and  $E_{\text{MnFe}_2\text{O}_4}$  are the DFT-calculated total energies of MnFe $_2\text{O}_4$  with and without Li intercalation, respectively, and  $E_{\text{Li}}$  is the energy of one Li atom in the bulk metal. To determine the favorable Li intercalation site, three types of vacancy sites for intercalation are considered: octahedral 16c, tetrahedral 48f, and tetrahedral 8b. The lowest formation energy occurs at the 16c octahedral sites for both the strained and unstrained materials (0.216 and 0.255 eV, respectively, Table S6), which is consistent with previous reports of preferential Li intercalation at the octahedral sites in spinel materials. The 0.04 eV energy difference suggests that Li intercalation is thermodynamically more favorable in the strained material. Moreover, the positive formation energies further support our claim that only reversible reactions take place in our materials during the electrochemical testing.

A qualitative comparison of the diffusion coefficients shows significant enhancement of the Li-ion diffusion rate in the strained samples. Since the rate at which Li-ions can intercalate and deintercalate depends on the kinetic properties of the Li-ions (i.e., Li diffusivity), nudged elastic band (NEB) calculations are carried out

to obtain the activation energy for Li diffusion between two adjacent 16c sites in the strained and unstrained lattices (site 4 and site 5, Table S6). Figure 5(c) shows the MnFe<sub>2</sub>O<sub>4</sub> supercell with the Li pathway from the initial site to the final site. A reduction in activation barrier for Li diffusion by 0.03 eV is observed in the strained lattice as compared to the *unstrained*-MnFe<sub>2</sub>O<sub>4</sub> [Fig. 5(b)]. The differences are measured between the maxima of both plots, where the local minima in both pathways pass through a tetragonal 48f site. The impact of activation energy differences on Li-ion diffusion is assessed through the qualitative comparison of diffusion coefficients calculated by the following Arrhenius equation:  $^{33}$ 

$$D = D_0 \cdot e^{(-\triangle E/kT)}, \tag{5}$$

where  $D_0$  is the constant pre-exponential term,  $\triangle E$  is the activation energy, k is Plank's constant, and T is temperature. By assuming that  $D_0$  is similar for both cases, the room temperature diffusion constant is found to be larger by a factor of 2.97 for the *strained*-MnFe<sub>2</sub>O<sub>4</sub> as compared to the *unstrained*-MnFe<sub>2</sub>O<sub>4</sub>. Although the differences in the formation and activation energies are small, this difference in activation energy results in a significant ( $\sim$ 3×) change in diffusion coefficients at room temperature.

The enhanced Li-ion diffusion rate in the strained-MnFe<sub>2</sub>O<sub>4</sub> electrodes predicted by the DFT results is further corroborated using GITT measurements. Determining the diffusion coefficient is generally difficult in Li-ion intercalation chemistry because the diffusion coefficient is dependent on the Li-ion concentration. GITT measures diffusion by applying short current pulses followed by a relaxation period to homogenize the Li-ion concentration in the active material. In the limit of low current density, the potential gradient across the active material is small and the diffusion can be modeled based on the single particle model.<sup>34–36</sup> For our GITT measurements, a current pulse of 0.2 A/g is applied for 30 s, and then, the cell equilibrates in an open circuit configuration for 2 min (Fig. 6, see the supplementary material for details). During the pulse periods, the voltage change in the strained-Fe<sub>3</sub>O<sub>4</sub>@ 2.70 nm-MnFe<sub>2</sub>O<sub>4</sub> is lower compared to the two unstrained electrodes [Fig. 6(b)], indicating superior reaction kinetics in the strained electrodes.<sup>37</sup> At the cell

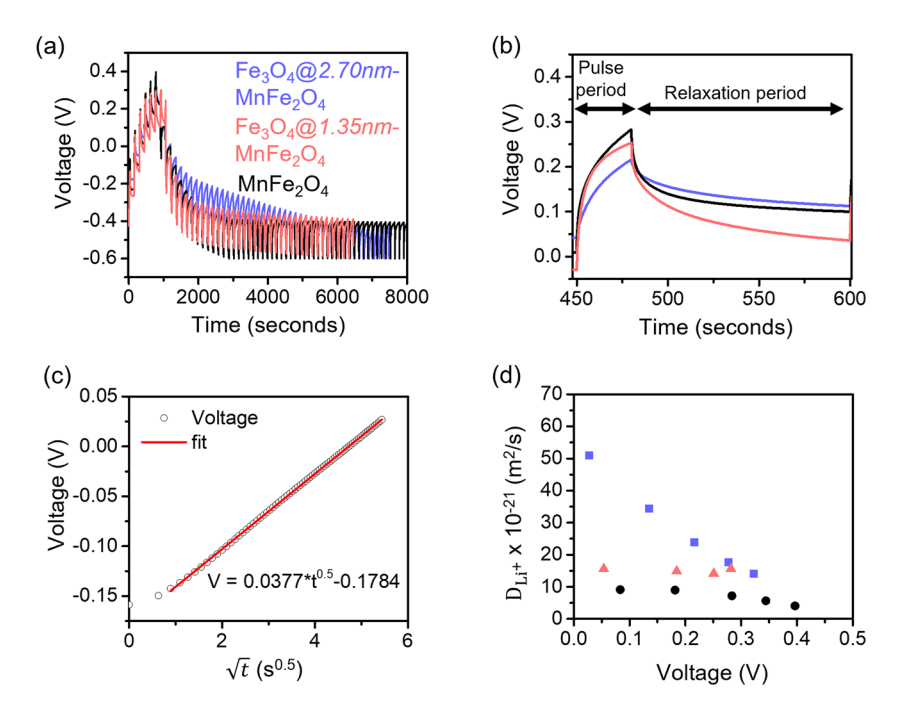


FIG. 6. Diffusivity of Li-ion calculated using the Galvanostatic Intermittent Titration technique (GITT). (a) Charging and discharging potential of Fe<sub>3</sub>O<sub>4</sub>@ 2.70 nm-MnFe<sub>2</sub>O<sub>4</sub> (blue), Fe<sub>3</sub>O<sub>4</sub>@ 1.35 nm-MnFe<sub>2</sub>O<sub>4</sub> (red), and unstrained-MnFe2O4 (black) electrodes derived GÍTT measurements. (b) Change in potential for one pulse cycle. (c) Linear behavior of the voltage vs square root of pulse time shown for one of the pulses during GITT measurement. (d) Li+ chemical diffusion coefficient  $(D_{\mathrm{Li}^+})$  as a function of the potential of the cell.

voltage of ~0.05 V,  $D_{Li^+} = 9.1 \times 10^{-21}$ ,  $15.6 \times 10^{-21}$ , and  $50.9 \times 10^{-21}$ m<sup>2</sup>/s for the unstrained-solid MnFe<sub>2</sub>O<sub>4</sub>, unstrained-Fe<sub>3</sub>O<sub>4</sub>@ 1.35 nm-MnFe<sub>2</sub>O<sub>4</sub>, and strained-Fe<sub>3</sub>O<sub>4</sub>@ 2.70 nm-MnFe<sub>2</sub>O<sub>4</sub>, respectively [Fig. 6(d) and Table S5]. A small deviation in the diffusion rate is observed in the unstrained-Fe<sub>3</sub>O<sub>4</sub>@ 1.35 nm-MnFe<sub>2</sub>O<sub>4</sub> compared to the unstrained-solid MnFe<sub>2</sub>O<sub>4</sub>, possibly due to small strain along different lattice planes [Fig. 3(b)]. On the contrary, the strained-Fe<sub>3</sub>O<sub>4</sub>@ 2.70 nm-MnFe<sub>2</sub>O<sub>4</sub> shows a significant 5.6× and 3.3× increase in the diffusion rate compared to the solid MnFe<sub>2</sub>O<sub>4</sub> and the Fe<sub>3</sub>O<sub>4</sub>@ 1.35 nm-MnFe<sub>2</sub>O<sub>4</sub> electrodes, respectively. These findings from GITT and DFT support the hypothesis that the strain facilitates the diffusion process and consequently improves the electrochemical performance of the strained-Fe<sub>3</sub>O<sub>4</sub>@ 2.70 nm-MnFe<sub>2</sub>O<sub>4</sub>. It should be noted that the surface area of the active material does not play a role in the electrochemical performance observed in our case. The thick-shelled samples have a bigger diameter compared to the solid MnFe<sub>2</sub>O<sub>4</sub> nanoparticles (8.30 vs5.6 nm); hence, the thick-shelled nanoparticle electrode has a lower surface area per unit mass. If the surface area were the dominant factor affecting the supercapacitor performance, a decrease in the supercapacitor performance should be observed with an increasing nanoparticle size. We observe an increase in performance with an increasing nanoparticle size, which confirms the hypothesis that the strain is the dominant factor affecting the electrochemical properties.

Theoretical calculations show that increasing the tensile strain in MnFe<sub>2</sub>O<sub>4</sub> can lead to further improvement in the electrochemical performance of the electrodes. On increasing the strain to 0.5%, a gradual reduction in both the formation energy for Li intercalation and activation barrier is observed (Fig. S8), which corresponds to an increase in the theoretical diffusion coefficient by a factor of ~5.4 as compared to the *unstrained*-MnFe<sub>2</sub>O<sub>4</sub>. On further increasing the tensile strain beyond 0.5% [Fig. S8(a)], the formation energies are negative, indicating a phase conversion during lithiation, which

could worsen the cyclability of the supercapacitor. Thus, although there is an inherent limit up to which the strain modification can help improve the electrochemical performance, we show experimentally that strain engineering can be used as an effective approach to improve the Li diffusion and consequently the supercapacitor performance of the electrodes.

In summary, we synthesize core@shell heterostructures and vary the shell thickness to control the strain in the MnFe<sub>2</sub>O<sub>4</sub> nanoparticles. We further show that strain engineering can be used as an effective strategy to modulate and improve the Li-ion transport kinetics as evident by an increase in the Li-ion diffusion constant as determined using GITT and DFT calculations and an increase in energy density by ~33%, power density by ~28%, and specific capacitance by ~48% for the  $strained\text{-MnFe}_2\text{O}_4$  electrodes. Ultimately, this work provides insight into the interplay between tunable strain and electrochemistry, thus providing a starting point to using strain engineering as a novel approach for designing high performance energy storage devices.

### SUPPLEMENTARY MATERIAL

The supplementary material is available free of charge containing the experimental methods and additional data for ICP-MS, XRD, XPS, TGA, electrochemical testing, and DFT + U (PDF).

### **ACKNOWLEDGMENTS**

This work was supported, in part, by the National Science Foundation (NSF) under Award Nos. DMR-1809429 and CMMI-1941135. This work made use of the Cornell Center for Materials Research (CCMR) facility and was funded, in part, by the National Science Foundation under Award No. DMR-1719875.

M.A.S. acknowledges support from the NSF GRFP under Award No. DGE-1650441. The FEI Titan Themis 300 was acquired through Grant No. NSF-MRI-1429155, with additional support from Cornell University, the Weill Institute, and the Kavli Institute at Cornell. Substrate preparation was performed, in part, at the Cornell NanoScale Facility, a member of the National Nanotechnology Coordinated Infrastructure (NNCI), which is supported by the NSF (Grant No. ECCS-1542081). This research was also supported by a grant from the United States-Israel Binational Science Foundation (BSF), Jerusalem, Israel, and the United States National Science Foundation (NSF). This research was supported by the Nancy and Stephen Grand Technion Energy Program (GTEP). This article is based upon the work from COST Action 18234, supported by COST (European Cooperation in Science and Technology). The authors also thank Shree Giri for helping with the ICP and Muhammad Salim for helping with the XPS experiments.

### **AUTHOR DECLARATIONS**

### **Conflict of Interest**

The authors declare no competing financial interest.

### **DATA AVAILABILITY**

The data that support the findings of this study are available from the corresponding author upon reasonable request.

### **REFERENCES**

- <sup>1</sup> J. Wang, J. Polleux, J. Lim, and B. Dunn, J. Phys. Chem. C 111, 14925 (2007).
- <sup>2</sup> A. M. Smith, A. M. Mohs, and S. Nie, Nat. Nanotechnol. **4**, 56 (2009).
- <sup>3</sup>K. Wen, K. H. L. Zhang, W. Wang, J. Lin, W. Lv, B. Wang, Z. M. Wang, J. H. Dickerson, X. Guo, and W. He, J. Power Sources 285, 37 (2015).
- <sup>4</sup>M. D. Bhatt and J. S. Lee, Int. J. Hydrogen Energy **42**, 16064 (2017).
- <sup>5</sup> H. Wang, S. Xu, C. Tsai, Y. Li, C. Liu, J. Zhao, Y. Liu, H. Yuan, F. Abild-Pedersen, F. B. Prinz, J. K. Nørskov, and Y. Cui, Science 354, 1031 (2016).
- <sup>6</sup>F. Ning, S. Li, B. Xu, and C. Ouyang, Solid State Ionics 263, 46 (2014).
- <sup>7</sup>C. Tealdi, J. Heath, and M. S. Islam, J. Mater. Chem. A 4, 6998 (2016).
- <sup>8</sup>N. Muralidharan, C. N. Brock, A. P. Cohn, D. Schauben, R. E. Carter, L. Oakes, D. G. Walker, and C. L. Pint, ACS Nano 11, 6243 (2017).
- <sup>9</sup> J. Wang, Y. Hu, B. Yang, X. Wang, J. Qin, and M. Cao, Nano Energy **87**, 106053
- <sup>10</sup>L. Oakes, R. Carter, T. Hanken, A. P. Cohn, K. Share, B. Schmidt, and C. L. Pint, Nat. Commun. 7, 11796 (2016).

- 11 P. Xiong, F. Zhang, X. Zhang, S. Wang, H. Liu, B. Sun, J. Zhang, Y. Sun, R. Ma, Y. Bando, C. Zhou, Z. Liu, T. Sasaki, and G. Wang, Nat. Commun. 11, 3297 (2020).
- 12 J. Hwang, Z. Feng, N. Charles, X. R. Wang, D. Lee, K. A. Stoerzinger, S. Muy, R. R. Rao, D. Lee, R. Jacobs, D. Morgan, and Y. Shao-Horn, Mater. Today 31, 100
- <sup>13</sup>B. T. Sneed, A. P. Young, and C.-K. Tsung, Nanoscale 7, 12248 (2015).
- <sup>14</sup>J. T. L. Gamler, A. Leonardi, X. Sang, K. M. Koczkur, R. R. Unocic, M. Engel, and S. E. Skrabalak, Nanoscale Adv. 2, 1105 (2020).
- <sup>15</sup>M. M. Thackeray, Adv. Energy Mater. 11, 2001117 (2021).
- <sup>16</sup>F. Rosciano, P. P. Pescarmona, K. Houthoofd, A. Persoons, P. Bottke, and M. Wilkening, Phys. Chem. Chem. Phys. 15, 6107 (2013).
- <sup>17</sup>C. Wei, Z. Feng, M. Baisariyev, L. Yu, L. Zeng, T. Wu, H. Zhao, Y. Huang, M. J. Bedzyk, T. Sritharan, and Z. J. Xu, Chem. Mater. 28, 4129 (2016).
- <sup>18</sup> A. Bhargava, R. Eppstein, J. Sun, M. A. Smeaton, H. Paik, L. F. Kourkoutis, D. G. Schlom, M. Caspary Toroker, and R. D. Robinson, Adv. Mater. 32, 2004490
- 19 A. Bhargava, C. Y. Chen, K. Dhaka, Y. Yao, A. Nelson, K. D. Finkelstein, C. J. Pollock, M. Caspary Toroker, and R. D. Robinson, Chem. Mater. 31, 4228 (2019). <sup>20</sup>S. D. Perera, X. Ding, A. Bhargava, R. Hovden, A. Nelson, L. F. Kourkoutis, and
- R. D. Robinson, Chem. Mater. 27, 7861 (2015). <sup>21</sup>O. O. Otelaja, D.-H. Ha, T. Ly, H. Zhang, and R. D. Robinson, ACS Appl. Mater. Interfaces 6, 18911 (2014).
- <sup>22</sup>D.-H. Ha, M. A. Islam, and R. D. Robinson, Nano Lett. **12**, 5122 (2012).
- <sup>23</sup>S. Sun, H. Zeng, D. B. Robinson, S. Raoux, P. M. Rice, S. X. Wang, and G. Li, J. Am. Chem. Soc. 126, 273 (2004).
- <sup>24</sup>K. Islam, M. Haque, A. Kumar, A. Hoq, F. Hyder, and S. M. Hoque, Nanomaterials 10, 2297 (2020).
- <sup>25</sup>Kurnia, Heriansyah, and E. Suharyadi, IOP Conf. Ser.: Mater. Sci. Eng. 202, 012046 (2017).
- <sup>26</sup> M. M. N. Ansari and S. Khan, *Physica B* **520**, 21 (2017).
- <sup>27</sup>B. Aslibeiki, P. Kameli, and M. H. Ehsani, Ceram. Int. **42**, 12789 (2016).
- <sup>28</sup> J. E. Spanier, R. D. Robinson, F. Zhang, S.-W. Chan, and I. P. Herman, *Phys.* Rev. B 64, 245407 (2001).
- <sup>29</sup> A. Nelson, Y. Zong, K. E. Fritz, J. Suntivich, and R. D. Robinson, ACS Mater. Lett. 1, 177 (2019).
- <sup>30</sup>T. Brousse, D. Bélanger, and J. W. Long, J. Electrochem. Soc. **162**, A5185 (2015). <sup>31</sup> W. Zhang, D. C. Bock, C. J. Pelliccione, Y. Li, L. Wu, Y. Zhu, A. C. Marschilok,
- E. S. Takeuchi, K. J. Takeuchi, and F. Wang, Adv. Energy Mater. 6, 1502471 (2016).
- 32 A. Van Der Ven, J. Bhattacharya, and A. A. Belak, Acc. Chem. Res. 46, 1216 (2013).
- <sup>33</sup>G. H. Vineyard, J. Phys. Chem. Solids 3, 121 (1957).
- <sup>34</sup> A. Nickol, T. Schied, C. Heubner, M. Schneider, A. Michaelis, M. Bobeth, and G. Cuniberti, J. Electrochem. Soc. 167, 090546 (2020).
- 35 S. Santhanagopalan, Q. Guo, P. Ramadass, and R. E. White, J. Power Sources **156**, 620 (2006).
- <sup>36</sup>M. Guo, G. Sikha, and R. E. White, J. Electrochem. Soc. 158, A122 (2011).
- <sup>37</sup>X. Yu, C. Zhang, Z. Luo, T. Zhang, J. Liu, J. Li, Y. Zuo, J. J. Biendicho, J. Llorca, J. Arbiol, J. R. Morante, and A. Cabot, Nano Energy 66, 104199 (2019).